Damage dynamics in single *E. coli* and the role of chance in the timing of cell death

Yifan Yang[1,2*], Omer Karin[1], Avi Mayo[1], Xiaohu Song[2], Peipei Chen[2], Ariel B. Lindner[2], Uri Alon[1*]

1 Dept. molecular Cell biology, Weizmann Institute, 71600 Rehovot, Israel

2 Université de Paris - INSERM Unit 1284, Center for Research and Interdisciplinarity (CRI), Paris F-75004, France.

Corresponding *

Genetically identical cells in the same stressful condition die at different times. The origin of this stochasticity is unclear; it may arise from different initial conditions that affect the time of demise, or from a stochastic damage accumulation mechanism that erases the initial conditions and instead amplifies noise to generate different lifespans. To address this requires measuring damage dynamics in individual cells over the lifespan, but this has rarely been achieved. Here, we used a microfluidic device to measure membrane damage in 648 carbon-starved *E. coli* cells at high temporal resolution. We find that initial conditions of damage, size or cell-cycle phase do not explain most of the lifespan variation. Instead, the data points to a stochastic mechanism in which noise is amplified by a rising production of damage that saturates its own removal. Surprisingly, the relative variation in damage drops with age: cells become more similar to each other in terms of relative damage, indicating increasing determinism with age. Thus, chance erases initial conditions and then gives way to increasingly deterministic dynamics that dominate the lifespan distribution.

Introduction

Genetically identical organisms placed in the same conditions die at different times [1–5]. This non-genetic variation is shared also by single celled organisms, such as starving *E. coli* [4] and aging yeast [6].

Two possibilities have been raised to understand this stochasticity of death times [1,2,7,8]. The first is that the initial states of individuals are different and affect the eventual time of demise [2,8]. The second is that initial conditions are rapidly erased by stochastic accumulation of damage over time, and stochasticity further accumulates to cause the different lifespans [7]. The nature of this stochastic accumulation is unclear.

To understand the role of chance and initial conditions in the timing of cell death, it is essential to measure the damage that causes death over time in individual cells. This, however, has rarely been done.

Here we use carbon-starved *E. coli* in microfluidic chambers to study the role of stochasticity and initial conditions in the time of cell death. The cells have a risk of death that rises exponentially with age [4], known as the Gompertz law, which also characterizes mortality in other microorganisms and animals [9]. We use the well-established bacterial viability marker propidium iodide [10] to measure membrane damage in individual cells in the microfluidic device. We find that initial conditions of damage or cell-cycle phase do not strongly correlate with time of death. Instead, the data suggests a specific mechanistic model for the stochastic dynamics of the damage that causes death. In this model, damage-producing units such as unfolded protein complexes rise at a constant rate and produce damage, whose removal processes saturate at high damage levels. This saturation amplifies noise and leads to widely different individual dynamics, explaining the majority of variation in lifespan. Surprisingly, the relative damage variation between cells drops with age, indicating that stochasticity erases initial conditions, but then becomes less dominant and damage dynamics becomes increasingly deterministic with age.

Results

E. coli damage dynamics in individual cells

We tracked individually starved *E. coli* cells by time-lapse microscopy using a microfluidic system called the mother machine [11] (Fig. 1A). Individual cells from the same clone were loaded onto an array of dead-end micro-channels (6μm long and 1.1μm high and wide) that open onto a main channel [12]. The micro-channels exposed the individual cells to a homogenous medium refreshed by flow in the main channel in which the cells were starved for carbon.

The device prevented cells from interacting. This bypasses the effects of feeding on the remains of perished cells that occur in batch culture starvation and lead to an exponential survival curve with a constant risk of death[13] rather than the Gompertz law observed in the microfluidic device[4]. To allow different initial cell-cycle phases and cell sizes, we loaded the cells onto the chip from a culture in exponential growth. Thus, some cells have recently divided whereas others are about to divide. The chip was then thoroughly washed to eliminate traces of carbon nutrient [4].

To follow the physiological deterioration process of each cell, we focused on membrane integrity as an indicator of damage. Membrane integrity is critical to a cell's survival [14–16] and is affected by many physiological parameters, including pH, redox balance, energy metabolism and translation fidelity [17].

We measured membrane integrity with propidium iodide (PI), a well-established non-toxic dye for bacterial viability [4]. PI becomes fluorescent only when it penetrates the cell membrane and binds to DNA. Due to its relatively large size and charge, PI can not cross the membrane when the membrane is functionally intact. We therefore used the rate of PI uptake to quantify the integrity of bacterial membranes (Fig. 1B). PI uptake rate was calculated from the image time-series of each bacterium at resolution of 1 hour (Methods). Experimental noise of the fluorescence image time-series is estimated at about 6% (SI Fig. S1).

According to the Arrhenius equation, PI uptake rate is inversely proportional to the exponential of the potential barrier that the PI molecule has to cross to enter the cell. We therefore define membrane damage X(t) as the log of the PI uptake rate normalized to the mean uptake rate of the initial population (Methods). Cell death was determined by damage levels exceeding a threshold, X_c. The value of X_c is determined by the maximal X(t) observed before cells reach previously established lifespans [4].

Cells survived for an average of 82h, and showed an exponentially rising risk of death (Fig. 1C), namely the Gompertz law [4]. Cells rarely die in the first 40 hours, and then begin to die more and more frequently, leading to a sigmoidal survival curve well described by a Weibull function (Methods). The relative variation of death times was 24%, where 5% of the cells died by 42h, and 95% died by 106h.

From the time-series of PI fluorescence we measured the damage X(t) in 648 individual bacterial cells at 8 time points, which correspond to 8 non-overlapping windows of 7 hours each between 20h and 80h. We do not consider the initial 20h period since it is a time over which cells adapt to the starvation conditions in the device, nor the data after 80 hours since most cells are dead.

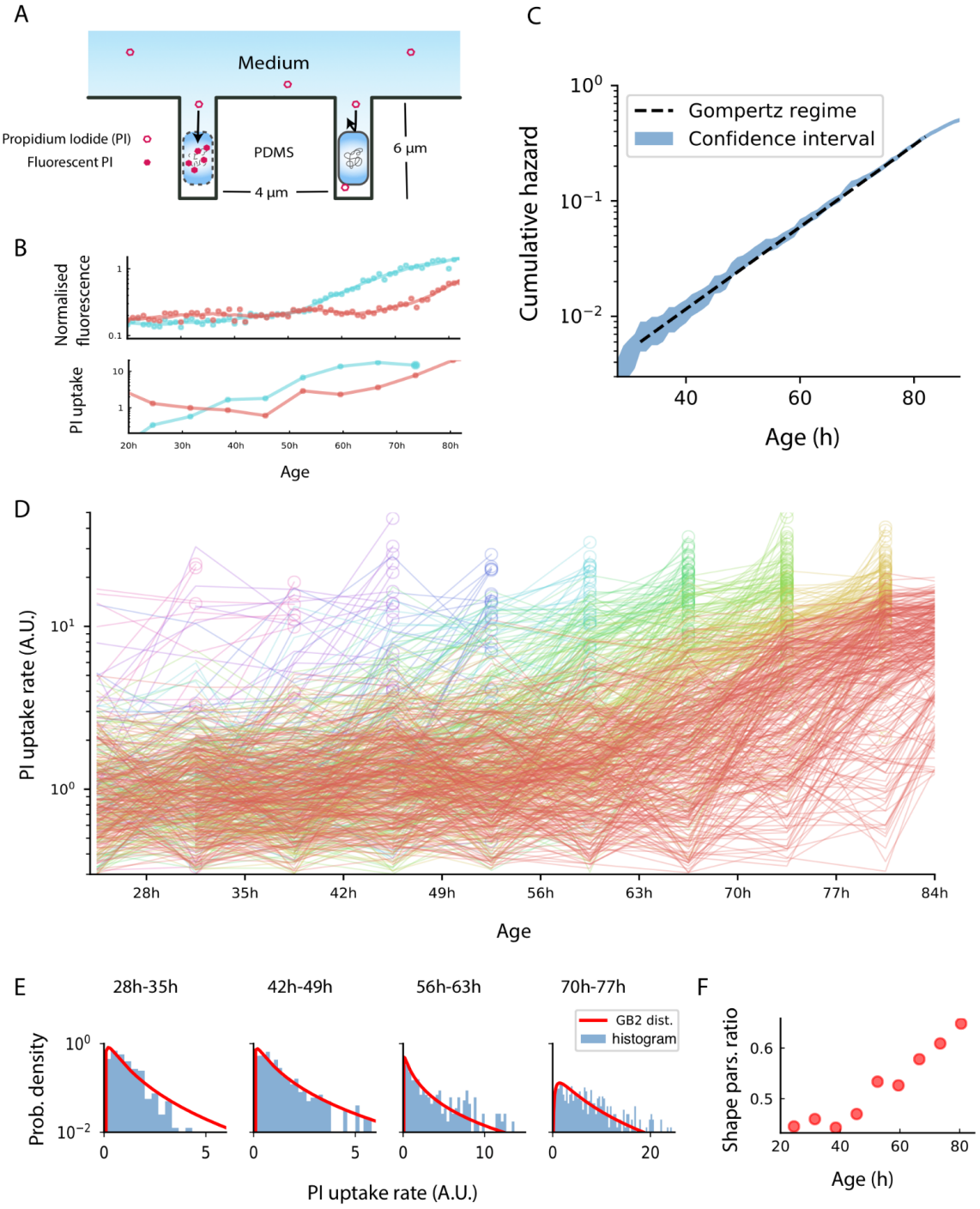

Fig. 1. Damage dynamics in starving *E. coli* cells. (**A**) Individual E coli cells were placed in microfluidic channels with medium flow. Propidium iodide (PI) was added to the medium as a proxy for membrane damage. PI only crosses the membrane and stains DNA when membrane integrity is compromised. (**B**) Membrane damage was measured by a temporal derivative of PI fluorescence, as

shown for two individual bacteria. Top: fluorescence signal, bottom: derivative (uptake rate) in 7h time windows. (**C**) Cumulative risk of death as a function of age shows an exponential regime. Cumulative risk of death is defined as negative natural logarithm of survivorship and is equal to the integral of the hazard function. The blue region corresponds to 95% confidence intervals. Death conditions are as previously defined [4]. (**D**) Cellular damage fluctuates around a rising trajectory, subsampled to 7h time windows. Trajectories are color coded by the time window of cell death, circles indicate the last time window before death to highlight the rise in damage leading to the point of death. (**E**) PI uptake rate distributions and best-fit to a type-2 generalized beta distribution with the ratio between shape parameters p/(p+q), plotted versus age in (**F**), see Methods.

Initial damage and cell-cycle phase do not correlate with lifespan in most cells

We asked whether initial conditions, namely the cell state when loaded onto the chip, might explain the variations in lifespan (Fig 2A). There was a negative correlation between initial damage and lifespan (Spearman $r=-0.41$, $p<0.001$). This correlation was primarily due to a subset of 3% of the cells that had high initial damage (PI uptake rate>4/h, compared to the mean uptake rate of 0.87/h in the remaining cells). These initially damaged cells had a short lifespan, averaging 48h.

We therefore divided the cells into two populations, with initial uptake rate above and below 4 (Fig. 2 B-C), which we call the high damage and low damage groups. The high damage group showed a strong correlation between initial damage and lifespan (Spearman $r=-0.70$, $n=17$, $p=0.002$). The low damage group, which comprised 95% of the cells, showed low correlation (Spearman $r=-0.15$, $n=503$, $p=0.001$).

We also investigated the effect of cell-cycle phases by noting the initial size of the cell and number and timing of reductive divisions on the chip[18]. We find that cell size has only weak correlations with lifespan (Spearman $r=-0.09$) (Fig. 2D), as did the time of last division (Spearman $r=-0.11$) (Fig. 2E) and number of divisions (Spearman $r=-0.06$).

Multiple regression shows that initial conditions explain a total of 27% of the variation for all cells, and 10% of the variation for the majority -- 95% of the cells -- with low initial damage (Fig. 2F). We conclude that in the traits measurable in this experiment, the initial conditions explain only a minority of the variation in lifespan.

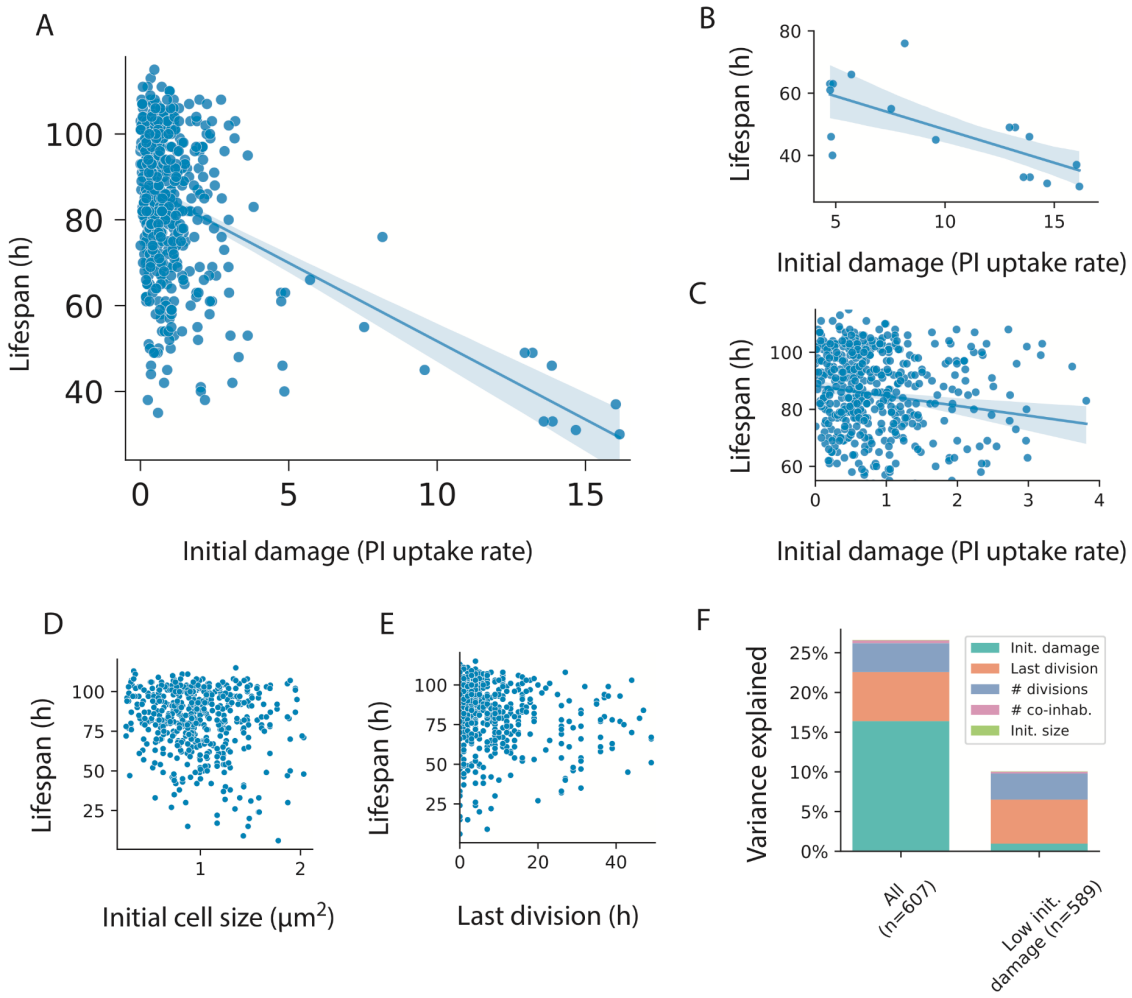

Fig. 2. Initial conditions do not account for most of the variations in lifespan. (**A**) Initial damage levels (PI uptake rate) and lifespan of all cells in the experiment; (**B**) For cells with high initial damage (PI uptake rate>4, n=18), initial damage correlates with lifespan; (**C**) For cells with low initial damage (<4, n=589), the correlation between initial damage and lifespan is weak; (**D**) Initial cell size and lifespan of all cells in the experiment; (**E**) Time of last division and lifespan for all cells in the experiment; (**F**) Fraction of lifespan variation explained by initial conditions according to multiple regression. Left are all cells, right are cells with low (<4) initial damage.

Damage dynamics rise and fall suggesting a stochastic mechanism

We next sought to characterize the stochastic dynamics of damage, defined as PI uptake rate, over time. Damage in each cell did not accumulate monotonically. Instead, damage rose and fell in each cell, with fluctuations larger than can be explained by experimental noise (Fig. 1D). This indicates that damage is produced and removed on the timescale of hours. These fluctuations occurred around a mean trajectory that accelerated with age on the scale of tens of hours. This suggests two timescales: in addition to the fast timescales of hours, a slower timescale of tens of hours over which damage production and removal rates change.

Notably, we find that cells become more similar in relative terms as they age. Although the mean damage and its standard deviation both rise with age (Fig. 3 A,B,F), the standard deviation rises more slowly than the mean. As a result, the relative variation drops with age, as measured by the coefficient of variation CV=SD/mean (Fig. 3C). 1/CV rose approximately linearly with age above 50h.

The increasing relative similarity between cells with age is seen also in the damage distributions at each timepoint. At early ages the distribution is skewed to the right, but skewness reduces with age (Fig. 3D), as the distribution becomes more symmetric,

The longitudinal nature of the data allowed us to calculate the autocorrelation of damage. Correlation time increased with age. This means that a cell with damage above or below the population average remained so for a longer at old ages (Fig. 3E). Plotting damage as a function of remaining lifetime shows that X=log(normalized PI uptake) becomes less dispersed the closer the cell is to death (Fig. 3G).

These findings indicate that the damage dynamics has aspects that become more deterministic with age.

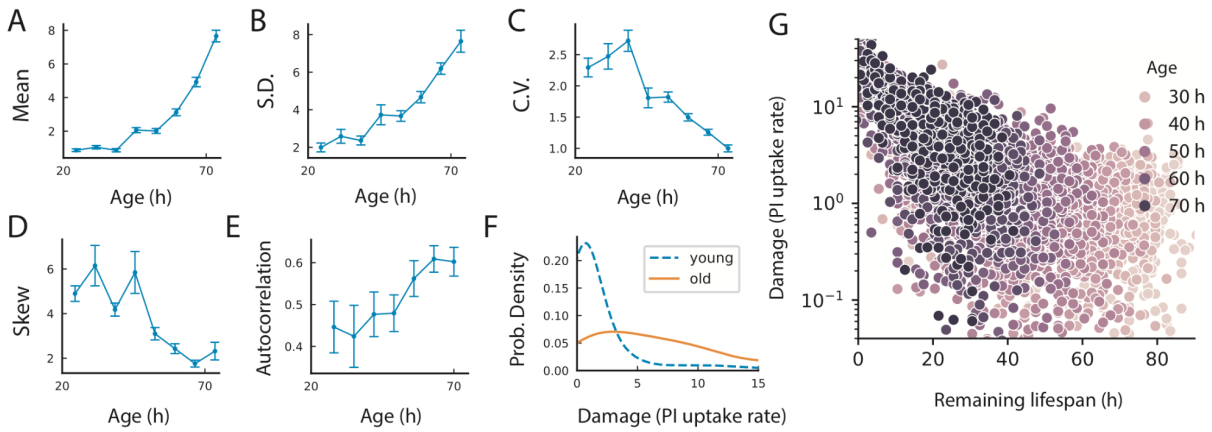

Fig. 3. Damage dynamics show increasing determinism with age. Statistics of *E. coli* membrane damage for all cells alive at a given age: Mean (**A**) and standard deviation (**B**) increase with age; but coefficient of variation (**C**) decreases, indicating reduced relative heterogeneity in the damage distribution. **(D)** Skewness drops with age. (**E**) Autocorrelation of damage increases with age, showing increasing persistence. (**F**) Probability distribution of damage in younger (52.5h blue dashed line) versus older (72.5h yellow solid line) cells. (**G**) Log PI uptake rate as a function of remaining lifespan becomes less variable close to death.

Damage dynamics indicate a saturated-repair stochastic model

To elucidate the stochastic mechanism that can give rise to these damage statistics, we modeled damage production and removal with noise. We exploited the separation of timescales in the data, namely the rapid fluctuations of damage around a slowly rising mean trajectory. Therefore, we explored models in which damage is produced and repaired quickly compared to the lifespan, whereas the rates of damage production and removal change slowly with age t (See Table S3 for relevant timescales). Damage removal and production were also allowed to depend on the amount of damage to include the possibility of feedback and saturation effects.

We use as a damage variable X=log(normalized PI uptake) to represent the loss of the free-energy barrier posed by the membrane in units of k_BT. We consider a general stochastic model dX/dt = production - removal + noise, or mathematically $dX/dt = G(X,t) + \sqrt{2\sigma}\xi$, where ξ is white noise of amplitude σ.

To define the production and removal terms that make up G(X,t), we used timescale separation, by assuming that at each time point the damage distribution among cells P(X,t) is a steady-state solution of the equation. The analytical solution for the steady-state is $P(X,t) = e^{-U(X,t)/\sigma}$, where U(X,t) is a potential function defined by $\partial U/\partial X = -G(X,t)$. This is analogous to the Boltzmann distribution in statistical mechanics.

Using the measured distribution of damage at different timepoints, P(X,t), we estimated U, integrated it to provide G(X,t) and hence the production-removal terms in the model.

To facilitate this process, we characterized the experimental damage distributions P(X,t) by comparing them to 15 commonly-used distribution functions with 3-4 parameters (SI Fig. S2, Table S1). The best fit for the PI uptake distribution was a type-2 generalized beta distribution[19] with shape parameters whose ratio, p/(p+q), rises approximately linearly with age (Fig. 1F). The stochastic process which gives rise to this distribution is (see Methods):

$$(1)\quad dX/dt = \eta t - \beta f(X) + \sqrt{2\sigma}\xi$$

In this inferred mechanism (Fig 4A) damage production rises linearly with age as ηt, and damage removal is a saturating function of damage, $\beta f(X) = \beta e^{aX}/(e^{aX} + e^{a\kappa})$, (Fig. 4B-C). The parameters are a production slope $\eta = (3.2 \pm 0.3) \times 10^{-3}\, k_BTh^{-2}$ and removal parameters $a =$

$0.33 \pm 0.03\ (k_BT)^{-1}$, $\beta = 0.48 \pm 0.02\ k_BTh^{-1}$ and $\kappa = 0.3 \pm 0.1\ k_BT$ The white noise amplitude is $\sigma = 0.1\ \pm 0.01(k_BT)^2\ h^{-1}$.

Notably, this model is in the same class as the saturated repair (SR) model established for aging in mice [20], in the sense that the production rate of damage rises linearly with age and damage inhibits or saturates its own removal. The only difference is that the mouse SR model used a different saturating removal function, $f(X) = X/(\kappa + X)$. Hence we call the model of Eq. 1 the membrane-potential-SR model or MP-SR model.

The MP-SR model captures the statistics of the observed PI uptake dynamics (Fig. 4D-G). It shows a reduction in the relative variation, CV=SD/mean (Fig. 4F), despite a super-linear rise in both mean and SD (Fig. 4D-E). The inverse CV, 1/CV, rises linearly with age as in the data. The model also captures the reducing skewness with age (Fig. 4G). Hence, the MP-SR model captures the dynamics of damage in the experiment.

To compute the distribution of lifespans in the MP-SR model, we modeled death as damage X exceeding a threshold X_c [20]. Death is therefore modeled as a first passage time process, which we computed numerically and analytically (Supplementary Information S4) using Kramer's approximation [21,22]. The model provides an exponential increase in the risk of death that slows at very old ages, namely the Gompertz law (Fig. 4H), and a Weibull-like sigmoidal survival curve (Fig. 4I), as experimentally observed. This Gompertzian exponential increase is due in the model to the linear rise in damage production, which causes the potential U to drop linearly with time; since crossing this barrier goes exponentially in U, the risk of death rises exponentially with time.

The differences in lifespan between individuals in the inferred stochastic mechanism is due to the fact that noise is effectively amplified by the saturation of damage removal. The slope of production minus removal becomes flat at old ages; fluctuations are not pulled back strongly towards equilibrium by the effective potential U (Fig. 4C). This is at the heart of how noise can generate different lifespans for cells with identical physiological parameters.

We conclude that PI-uptake trajectories and their reducing relative variation are well-explained by an SR-type model in which damage production (loss of membrane barrier function) rate rises linearly with age whereas damage removal saturates.

This SR-type model makes a further prediction that may be called ‘shortening twilight’ [23,24]. Twilight is the remaining lifespan after a given damage threshold is crossed, and the SR model

predicts that twilight shortens with age. This shortening twilight prediction is borne out by the *E. coli* damage data (SI Fig. S3).

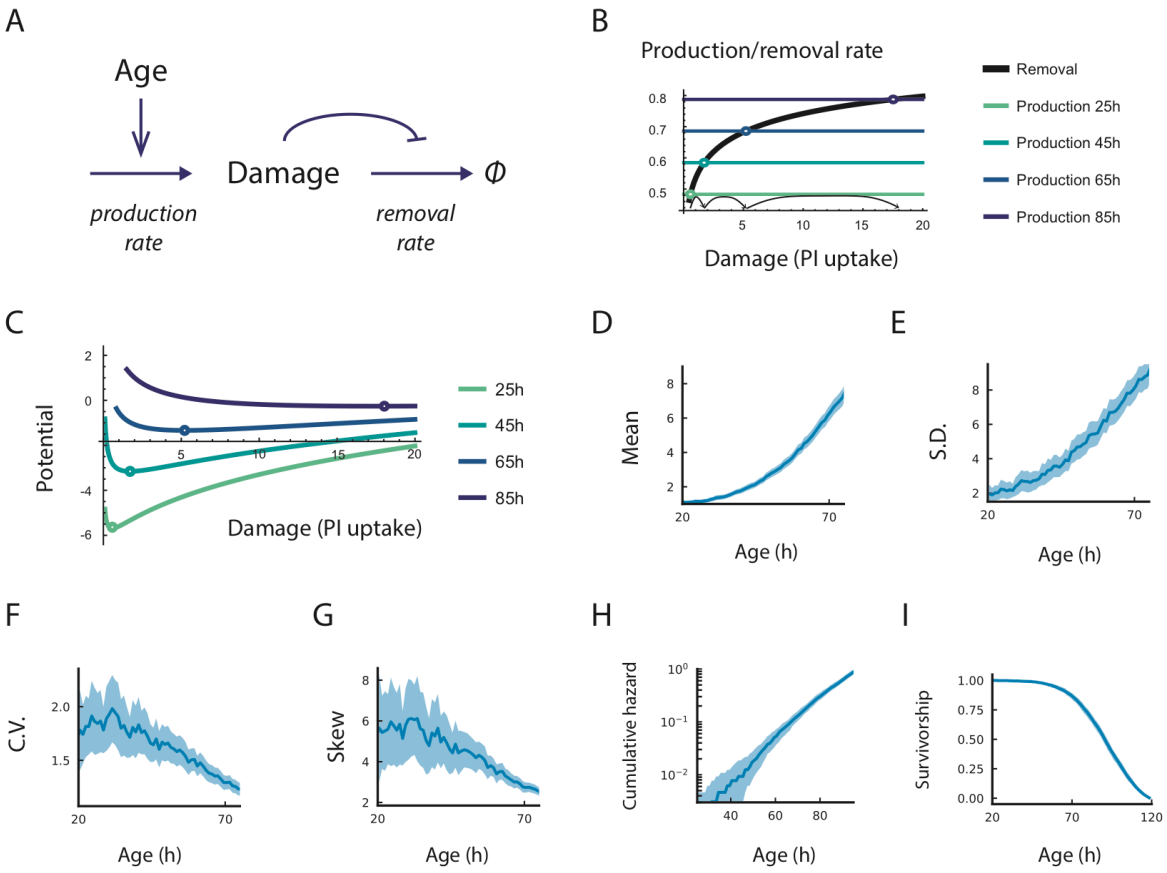

Fig 4. The saturating-removal model captures damage dynamics. (**A**) Schematic of the MP-SR model. (B) rate plot showing linearly increasing production with age and a removal rate that saturates with damage, causing the fixed point to accelerate to high damage levels. (**C**) The potential function of the MP-SR model and its evolution with age. Simulations of the MP-SR model for PI uptake rate (e^X) show rising mean (**D**) and standard deviation (**E**), reducing CV (**F**) and reducing skewness (**G**). The model provides a death hazard that rises exponentially with age (**H**) and a Weibull-like survival function (**I**). Blue regions are 95% confidence intervals from simulation of N=645 cells.

Discussion

We studied the role of chance and initial conditions on lifespan by measuring membrane damage over time in starved *E. coli* cells in a microfluidic device. Initial conditions in each cell, such as initial damage, cell size or cell-cycle phase, did not strongly correlate with time of death in most cells. Instead, damage fluctuated in each cell around a rising mean trajectory. Unexpectedly, the relative variation in damage dropped with age. This indicates an increasing determinism with age, where damage levels become more similar in relative terms the older the cells are. Correlation times increased and distributions became less skewed, further indicating rising determinism.

We used our dynamical damage measurements to infer a stochastic mechanism that provides the dynamics and survival curves. In this mechanism, damage is produced at a rate that rises linearly with age, and damage-removal saturates at high damage levels. We called the mechanism the membrane-potential saturating repair (MP-SR) model. Our findings suggest that chance fluctuations, amplified by saturating removal of damage, play a major role in explaining why genetically identical bacterial cells in the same conditions die at different times.

The damage dynamics measured here have statistical features that differ from random walks and from most previously suggested models of aging [25–27]. The mean rises faster than the standard deviation, so that the relative heterogeneity between cells at a given age declines. This can be quantitated as a drop in the coefficient of variation, CV=SD/mean, such that 1/CV rises roughly linearly with age. This is an unusual feature in stochastic processes in general, and in previous theoretical models of aging including network models [25,26], the Strehler-Mildvan model [27], the cascading failure model [7], fixed frailty model [8] and Ornstein-Uhlenbeck type models which do not provide a drop in damage CV with age but instead have a constant CV (SI).

The present MP-SR mechanism has two main features that require biological explanations. The first feature is the linear rise with age of the damage production rate, ηt . This linear rise can be explained by assuming that damage arises from ‘damage-producing units’, such as unfolded-protein complexes, that are added at a constant rate and cannot be resolved or removed [28–34]. If these complexes assimilate new unfolded proteins at a constant rate, and can not be removed,

their total mass should rise linearly with time. Such unfolded protein complexes are known to be toxic to cells [31]; they cause damage such as dysregulated proteostasis [35], which can lead to membrane damage [36,37].

Mathematically, if cells accumulate damage-producing units P at a constant rate v, and these units cannot be removed, their number rises linearly with age, $P = v\,t$. Each unit produces damage at rate b, so that total damage production rate rises linearly with time as ηt with $\eta = v\,b$ Organisms that manage to dilute such damage-producing units P, such as organisms with indefinite growth, are predicted to have different damage dynamics, in which P does not rise indefinitely. Such dilution occurs in growing and dividing bacterial cells [31,32], but not in the non-growing starved cells studied here. Other examples of damage dilution may occur in eukaryotic cells with symmetric division such as fission yeast; in contrast, budding yeast with asymmetric divisions show aging and eventual death of the mother cell which retains damage rather than passing it to daughter cells.

The second feature of the MP-SR model is the saturation of damage removal, which is crucial for the present dynamical hallmarks. The relevant removal mechanisms in *E coli* include chaperones and proteases [35], as well as enzymatic systems that repair proton leakage [38], oxidative damage [39] and maintain membrane structural integrity [40]. Such enzymatic repair mechanisms should naturally saturate at high damage levels.

Notably, the inferred stochastic mechanism in *E. coli* is similar to a mechanism inferred in the context of mice aging by Karin *et al*. Karin *et al* used stochastic trajectories of senescent cells in mice, cells which are growth arrested cells that cause inflammation, to infer a mechanism for senescent-cell accumulation [20]. This mechanism, called the saturating removal (SR) model, is a stochastic differential equation with a production rate that rises linearly with age and a removal rate that saturates, so that high senescent cell levels slow their own removal. Karin *et al* experimentally confirmed a prediction of the SR model, that senescent cell turnover slows with age [20]. The SR model was generalized to other forms of damage, and explains observations on aging such as the Gompertz law, heterochronic parabiosis [41], age-related disease incidence in

humans [42] and the scaling of survival curves in *C. elegans* [5,20]. Interestingly, the human frailty index shows similar dynamical features, including a reduction in CV with age [43].

The similarity between the present study on *E. coli* cells and the model of Karin *et al* on mammalian aging hints at a possible universality in mechanisms of aging, in which chance plays a large role in the differing lifespans of genetically identical organisms. Although the molecular forms of damage and lifespan timescales are very different between *E. coli* and mice, the features of linearly rising production and saturating removal may be more general and give rise to similar damage dynamics, with reducing relative heterogeneity with age.

It would be interesting to measure longitudinal damage trajectories in other organisms to explore whether linear-production-and-saturating-removal models might apply more generally. In the context of bacteria, it would be important to explore the dynamics of damage in cells challenged with antibiotics, in order to better understand the role of chance in the function of these drugs.

Acknowledgement

We thank Valery Krizhanovsky for discussions, Nicholas Stroustrup for discussion and sharing data on shortening twilight, David S. Glass for general discussions and editing help. Warm thanks to Chantal Lotton for technical lab support.

Author contributions: Conceptualization: YY, OK, ABL, UA; Methodology: YY, OK, AM, ABL, UA; Investigation: YY, AB; Software: XS; Resources: PC, ABL; Data curation: YY, AB; Formal analysis: YY, AM, UA; Visualization: YY, UA; Writing – original draft: YY, UA; Writing – review & editing: YY, UA.

Funding: European Research Council (ERC) grant agreement No 856487 (UA); Axa Foundation Longevity Chair (ABL., INSERM U1284); Bettencourt Schueller Foundation (FBS) (ABL., INSERM U1284).

Competing interests: The authors declare no competing interests.

References

1. Kirkwood, T. B. L. *et al.* What accounts for the wide variation in life span of genetically identical organisms reared in a constant environment? *Mech. Ageing Dev.* **126**, 439–443 (2005).
2. Finch, C. E. *et al. Chance, Development, and Aging*. (Oxford University Press, 2000).
3. Rea, S. L., Wu, D., Cypser, J. R., Vaupel, J. W. & Johnson, T. E. A stress-sensitive reporter predicts longevity in isogenic populations of Caenorhabditis elegans. *Nat. Genet.* **37**, 894–898 (2005).
4. Yang, Y. *et al.* Temporal scaling of aging as an adaptive strategy of Escherichia coli. *Sci. Adv.* **5**, eaaw2069 (2019).
5. Stroustrup, N. *et al.* The temporal scaling of Caenorhabditis elegans ageing. *Nature* **530**, 103–107 (2016).
6. Li, Y. *et al.* A programmable fate decision landscape underlies single-cell aging in yeast. *Science* **369**, 325–329 (2020).
7. Le Bras, H. Lois de mortalité et âge limite. *Population* **31**, 655–692 (1976).
8. Vaupel, J. W. & Missov, T. I. Unobserved population heterogeneity: A review of formal relationships. *Demogr. Res.* **31**, 659–686 (2014).
9. Jones, O. R. *et al.* Diversity of ageing across the tree of life. *Nature* **505**, 169–173 (2014).
10. Ericsson, M., Hanstorp, D., Hagberg, P., Enger, J. & Nyström, T. Sorting Out Bacterial Viability with Optical Tweezers. *J. Bacteriol.* **182**, 5551–5555 (2000).
11. Wang, P. *et al.* Robust growth of Escherichia coli. *Curr. Biol. CB* **20**, 1099–1103 (2010).
12. Yang, Y., Song, X. & Lindner, A. B. Chapter 2 - Time-lapse microscopy and image analysis of Escherichia coli cells in mother machines. in *Methods in Microbiology* (eds. Harwood, C. & Jensen, G. J.) vol. 43 49–68 (Academic Press, 2016).
13. Schink, S. J., Biselli, E., Ammar, C. & Gerland, U. Death Rate of E. coli during Starvation Is Set by Maintenance Cost and Biomass Recycling. *Cell Syst.* **9**, 64-73.e3 (2019).
14. Baquero, F. & Levin, B. R. Proximate and ultimate causes of the bactericidal action of antibiotics. *Nat. Rev. Microbiol.* **19**, 123–132 (2021).
15. Schink, S. *et al.* The energy requirements of ion homeostasis determine the lifespan of starving bacteria. 2021.11.22.469587 Preprint at https://doi.org/10.1101/2021.11.22.469587 (2021).
16. Wong, F. *et al.* Cytoplasmic condensation induced by membrane damage is associated with antibiotic lethality. *Nat. Commun.* **12**, 2321 (2021).

17. Benarroch, J. M. & Asally, M. The Microbiologist's Guide to Membrane Potential Dynamics. *Trends Microbiol.* (2020) doi:10.1016/j.tim.2019.12.008.
18. Nyström, T. Stationary-phase physiology. *Annu. Rev. Microbiol.* **58**, 161–181 (2004).
19. McDonald, J. B. Some Generalized Functions for the Size Distribution of Income. *Econometrica* **52**, 647–663 (1984).
20. Karin, O., Agrawal, A., Porat, Z., Krizhanovsky, V. & Alon, U. Senescent cell turnover slows with age providing an explanation for the Gompertz law. *Nat. Commun.* **10**, 5495 (2019).
21. Berglund, N. Kramers' law: Validity, derivations and generalisations. Preprint at https://doi.org/10.48550/arXiv.1106.5799 (2013).
22. Kramers, H. A. Brownian motion in a field of force and the diffusion model of chemical reactions. *Physica* **7**, 284–304 (1940).
23. Zhang, W. B. *et al.* Extended Twilight among Isogenic C. elegans Causes a Disproportionate Scaling between Lifespan and Health. *Cell Syst.* **3**, 333-345.e4 (2016).
24. Oswal, N., Martin, O. M. F., Stroustrup, S., Bruckner, M. A. M. & Stroustrup, N. A Hierarchical Process Model Links Behavioral Aging and Lifespan in C. elegans. 2021.03.31.437415 Preprint at https://doi.org/10.1101/2021.03.31.437415 (2021).
25. Vural, D. C., Morrison, G. & Mahadevan, L. Aging in complex interdependency networks. *Phys. Rev. E* **89**, 022811 (2014).
26. Kaplan, Y. *et al.* Observation of universal ageing dynamics in antibiotic persistence. *Nature* **600**, 290–294 (2021).
27. Strehler, B. L. & Mildvan, A. S. General Theory of Mortality and Aging. *Science* **132**, 14–21 (1960).
28. Schramm, F. D., Schroeder, K. & Jonas, K. Protein aggregation in bacteria. *FEMS Microbiol. Rev.* **44**, 54–72 (2020).
29. Ben-Zvi, A., Miller, E. A. & Morimoto, R. I. Collapse of proteostasis represents an early molecular event in Caenorhabditis elegans aging. *Proc. Natl. Acad. Sci. U. S. A.* **106**, 14914–14919 (2009).
30. Labbadia, J. & Morimoto, R. I. The Biology of Proteostasis in Aging and Disease. *Annu. Rev. Biochem.* **84**, 435–464 (2015).
31. Lindner, A. B., Madden, R., Demarez, A., Stewart, E. J. & Taddei, F. Asymmetric segregation of protein aggregates is associated with cellular aging and rejuvenation. *Proc. Natl. Acad. Sci.* **105**, 3076–3081 (2008).
32. Proenca, A. M., Rang, C. U., Qiu, A., Shi, C. & Chao, L. Cell aging preserves cellular immortality in the presence of lethal levels of damage. *PLOS Biol.* **17**, e3000266 (2019).

414 33. David, D. C. *et al.* Widespread protein aggregation as an inherent part of aging in C.
415 elegans. *PLoS Biol.* **8**, e1000450 (2010).
416 34. Moreno, D. F. *et al.* Proteostasis collapse, a hallmark of aging, hinders the chaperone-Start
417 network and arrests cells in G1. *eLife* **8**, e48240 (2019).
418 35. Santra, M., Farrell, D. W. & Dill, K. A. Bacterial proteostasis balances energy and chaperone
419 utilization efficiently. *Proc. Natl. Acad. Sci.* **114**, E2654–E2661 (2017).
420 36. Kohanski, M. A., Dwyer, D. J., Wierzbowski, J., Cottarel, G. & Collins, J. J. Mistranslation of
421 membrane proteins and two-component system activation trigger antibiotic-mediated cell
422 death. *Cell* **135**, 679–690 (2008).
423 37. Akiyama, Y. Quality control of cytoplasmic membrane proteins in Escherichia coli. *J.*
424 *Biochem. (Tokyo)* **146**, 449–454 (2009).
425 38. Kobayashi, R., Suzuki, T. & Yoshida, M. Escherichia coli phage-shock protein A (PspA)
426 binds to membrane phospholipids and repairs proton leakage of the damaged membranes.
427 *Mol. Microbiol.* **66**, 100–109 (2007).
428 39. Denoncin, K. *et al.* A new role for Escherichia coli DsbC protein in protection against
429 oxidative stress. *J. Biol. Chem.* **289**, 12356–12364 (2014).
430 40. Nakayama, T. & Zhang-Akiyama, Q.-M. pqiABC and yebST, Putative mce Operons of
431 Escherichia coli, Encode Transport Pathways and Contribute to Membrane Integrity. *J.*
432 *Bacteriol.* **199**, e00606-16 (2017).
433 41. Karin, O. & Alon, U. Senescent cell accumulation mechanisms inferred from parabiosis.
434 *GeroScience* **43**, 329–341 (2021).
435 42. Katzir, I. *et al.* Senescent cells and the incidence of age-related diseases. *Aging Cell* **20**,
436 e13314 (2021).
437 43. Rockwood, K. & Mitnitski, A. Frailty in Relation to the Accumulation of Deficits. *J. Gerontol.*
438 *Ser. A* **62**, 722–727 (2007).
439

Methods

Experimental and analytical methods

Microfluidic chip fabrication. The negative master mould for the modified mother machines was fabricated on top of silicon wafers in two steps. First, arrays of dead-end channels (2000x 6 µm long) were fabricated via electron-beam lithography (EBL) in a specialized micro-fabrication facility. It was necessary to use EBL for these channels due to the high precision requirements for the cross section dimensions (both height and width have to be between 1.1 and 1.2 µm). They had to be large enough to allow single cells to enter yet narrow enough so that multiple cells could not be squeezed in the same channel. In the second step, using standard photolithography methods, the negative mould for the main channel was overlaid perpendicular to the dead-end channels. The main channel is 10mm long, 50µm wide and 10µm deep.
For each run of the bacterial starvation experiment, microfluidic chips were fabricated by casting PDMS structures out of negative master moulds. Uncured PDMS mixes (RTV-615, Momentive Performance Materials) were poured to a thickness of 3mm onto the silicon wafer carrying the master moulds, and then de-gassed under vacuuming and spread out via gravity for about 2 hours. The PDMS was then partially heat cured at 80°C for about an hour to form solid yet flexible PDMS blocks with patterned surfaces. After drilling inlets and outlets through the flow channel, the PDMS blocks were bound to cover glasses suitable for microscopy, using oxygen plasma (90 s, 1000 mTorr). Lastly, the assemblies were cured fully at 80°C overnight and so that the PDMS structure was sealed permanently to the glass cover slide.
On the day of the experiment, the microfluidic chip was again treated by oxygen plasma for 90s so that its surfaces were activated, and then injected with 20% (v/v) polyethylene glycol 400 solution for at least 1h to prevent bacterial adhesion.

Material and equipment. During the process of media preparation, sterilization, cell culture and fluidic infusion, we generally avoided disposable lab plasticware in favor of glass or equipment whose wetted surfaces are coated with fluoropolymer such as polytetrafluoroethylene (PTFE). This step avoided a pitfall in which trace concentrations of carbon and energy-rich chemicals leached into the media, such as phthalate plasticisers commonly used in PVC tubings. Such

compounds can serve as carbon sources and allow the cells to grow, circumventing the goal of our experiments [4]. Medium was filter-sterilized (0.2 μm) to avoid contamination by volatiles during autoclaving, and glassware was sterilized by dry heat. In the mother machine chips we subjected a relatively small number of cells (<10,000) to constantly refreshing volumes (5 μl per hour) of media.

Bacterial growth and loading. Bacterial cultures were loaded into the microfluidic chip via centrifugation. All culture media were filter-sterilized before use to remove dust particles, which might otherwise block the microfluidic channels. *E. coli* wildtype strain MG1655 with a chromosomal-inserted constitutively CFP-expressing cassette (PrrnB2) was grown overnight in M9 minimal media (supplemented by 2mM MgSO4, and 0.1 mM CaCl2) at 37°C with 40mM succinate as carbon source, and diluted 250 fold into 50ml of the same media in 250-ml Erlenmeyer flasks. This subculture was grown to exponential phase (OD600 ~ 0.1) at 37°C and then transferred to glass centrifugation tubes and harvested by centrifugation at 4000rpm for 15min. The bacterial pellet was resuspended, washed with fresh carbon-free M9 media and centrifuged 3 more times. The resulting pellet was resuspended a final time with 20μl M9 media. This final suspension was manually injected into the main channel of the microfluidic chip, and forced into the dead-end channels by centrifugation at 1000rpm for 15min. After centrifugation, the main channel is washed thoroughly by carbon-free M9 media to remove all cells that remain there.

Microfluidic and microscopy setup. After the microfluidic chip was loaded with cells, it was connected to a linear, flow-controlled fluidic system driven by a high-precision syringe pump (Harvard Apparatus PHD 2000 Programmable) and GC-grade glass/PTFE syringes (Hamilton Gaslight 1000 series). As mentioned previously, PTFE tubing and glass syringes are used to avoid leaching of plasticizers into the media. This is critical for this type of microfluidic starvation experiments, as *E. coli* are able to uptake as carbon sources the trace concentrations of plasticizers in the media when it is constantly refreshed by the microfluidic flow. The syringes are preloaded with filter-sterilized M9 minimal media without carbon source, supplemented with propidium iodide (PI, 5 μg/ml). The chip was first washed at 100μl per hour for 30 min and then the flow rate was halved every 15 min to a final flow rate of 5μl per hour. In the meantime, the

chip was mounted and stabilized onto the objective stage of an inverted microscope (Nikon ECLIPSE Ti2, 100× oil-immersion objective, controlled with MetaMorph software) with temperature controlled at 37°C. Phase-contrast and fluorescence (PI signal excitation, 546/12 nm; emission, 605/75 nm; CFP excitation 436/20nm; emission 480/40nm) images were automatically taken for up to 90 imaging positions every hour for up to 120 hours. Focus was maintained by the hardware-based Perfect Focus System (PFS) from Nikon.

Image analysis. We used a published image analysis method specifically designed for mother machines [12]. The regions in the time-lapse images of each dead-end channel were detected and cut out of the image stacks and displayed chronologically from left to right on the same image. Cells were segmented using the CFP (constitutively expressed) fluorescent image. The segmentation approach was semi-automatic and consisted of automatic segmentation, lineage assignment and manual correction. First, the central region of the cells was detected using statistical p-value thresholding, assuming that the observed intensities are spatially distributed as Gaussian functions. Then these central regions were used as seeds to add recursively neighboring points with similar intensities to form labeled regions. The result of this automatic process is an accurately segmented image with occasional over segmentation errors. Then labeled regions from different time points in the same dead-end channels were assigned together with arrows to track the same cell through time. These automatically segmented and tracked cells are then manually corrected to account for over-segmentation errors and mis-assignment due to sudden movements of the cells. For more details see [12]. For each segmented and tracked cell through time, we used the segmented CFP contours to extract the average PI fluorescence signal.

Modeling and statistical methods

Measurements of membrane damage. Our general approach is to use the time derivative of fluorescence to calculate the rate constant of PI uptake, which in turn is a proxy for membrane damage.

We model the PI fluorescence time series with one slow and one fast chemical reaction. The slow reaction is PI uptake $PI_{ext} \rightarrow PI_{in}$ with rate constant r, and the fast reaction is PI binding to

DNA once inside the cell $[PI]_{in} + [DNA] \Leftrightarrow [PI{:}\,DNA]$, assumed reversible and at equilibrium with equilibrium constant K, so that $K[DNA][PI]_{in} = [PI{:}\,DNA]$.

First we focus on the rate of PI uptake. The Arrhenius equation states that the logarithm of the rate constant scales linearly with activation energy, in this case, an energetic barrier representing the integrity of the cell membrane. Thus we defined membrane damage X(t) as the reduction of this energy barrier compared to a healthy baseline. X(t) has the unit of k_BT, where T is the experimental temperature 310K and k_B is the Boltzmann constant. We can choose the unit appropriately, i.e. to be k_BT, X(t) can be made unitless. Under these definitions, the rate constant is $r = A_0 e^{X(t)}$, where T is the experimental temperature 310K and k_B is the Boltzmann constant. Then the PI uptake rate is $A_0 e^{X(t)}([PI]_{ext} - [PI]_{in})$.

Having defined the relation between membrane damage and PI uptake rate, our task is the estimation of the latter using fluorescence time-series. Since PI only becomes fluorescent when bound to DNA, average fluorescence intensity is proportional to the bound form of PI: $[Fluo] = J_F[PI{:}\,DNA]$. Since the binding of PI to DNA is assumed to be at equilibrium, we have $[PI{:}\,DNA] = ([PI]_{in} + [PI{:}\,DNA])\frac{K[DNA]}{1+K[DNA]}$. Thus the time derivative of fluorescence should be proportional to the PI uptake rate:

$$\frac{d[Fluo]}{dt} = A_0 e^{X(t)}([PI]_{ext} - [PI]_{in})\frac{J_F K[DNA]}{1+K[DNA]}.$$

To obtain relative fluorescence time-series we normalize for each cell its fluorescence signal $[Fluo]$ by its observed maximum $[Fluo]_{max} = J_F K[DNA][PI]_{ext}$. The relative time series is thus $s(t) = [Fluo]/[Fluo]_{max} = [PI]_{in}/[PI]_{ext}$. Membrane damage can be calculated from the experimentally observed relative fluorescence $s(t)$:

$$\frac{ds(t)}{dt} = \frac{d[Fluo]}{dt}/[Fluo]_{max} = \frac{A_0 e^{X(t)}}{1 + K[DNA]}[1 - s(t)]$$

and thus we obtain the formula used in our analysis

$$A_1 e^{X(t)} = \frac{ds(t)/dt}{1-s(t)},$$

where $A_1 = A_0/(1 + K[DNA])$.

A_1 is an Arrhenius-type pre-exponential factor with a unit of inverse time. It is assumed to be constant, because DNA concentration should be constant among the non-growing cells in our

experiment. The value of A_1 is not relevant to the dynamics of damage, thus we used A_1 ==1/600 so that initial timepoints start close to PI uptake rates of 1.

Time-series analysis and numerical differentiation. The fluorescence series was zeroed by the background and then divided by the maximum fluorescence for each cell to arrive at *s(t)* defined above. To arrive at estimates for PI uptake rate, $\frac{ds(t)/dt}{1-s(t)}$, we performed numerical differentiation of *s(t)* in a fashion that reduces the impact of experimental noise. In the present time-lapse microscopy experiments where single cells inside microfluidic chambers are imaged, experimental noise is driven by fluctuations in focus on the z-axis. This type of noise is approximately multiplicative and non-correlated in neighboring 1h time points (see Fig. S1). We therefore smoothed the log-transformed data *ln[s(t)]* in time windows of 7h with a Wiener filter. Then *dln[s(t)]/dt* were estimated using linear regression in non-overlapping 7h windows. The resulting time derivatives are multiplied by the *s(t)/[1-s(t)]* to arrive at $A_1 e^{X(t)}$.
The typical values of X(t) during the lifetime of the bacteria begin around 0.01Xc and rise to cross Xc at 80-100h.

Marginal damage distributions. We searched for an analytical form for the probability distribution function that can fit the damage distributions at various ages with age-dependent parameters. We tested 15 commonly used probability distributions. Each distribution has a probability density function f(Z/σ; Θ), where Z is the value of the random variable, Θ is the vector for the shape parameters and σ is the scaling parameter. We fit this to the empirical damage distribution Z_{it} of cell i at age t, by maximizing the likelihood $\Sigma_i f(Z_{it}/\sigma_t; \Theta_t)$ as a function of parameters σ_t, Θ_t, using the scipy.stats package of python. The goodness of fit was evaluated by the one-sample Kolmogorov-Smirnov (K-S) test. The tested distributions, the K-S test statistics and associated p-value are shown in Table S1 and Figure S1.
The three distribution functions that best fit the marginal damage distributions, Burr, Burr12 and Fisk, are all special cases of the generalized beta distribution of the second kind (GB2) [19], whose probability density function is:

$$f_{GB2}(Z) = a\, b^{aq}\, Z^{ap-1}(b^a + Z^a)^{-p-q} \quad /Beta(p,q),$$

where p and q are dimensionless shape parameters, and a and b describe the cooperativity and scale of the observed damage proxy Z, the PI uptake rate. GB2 becomes a Burr (Burr Type III) distribution when q=1 and a Burr12 distribution when p=1, and the Fisk distribution when p=q=1. Since the damage we seek is X=ln(Z), we transform to obtain:

$$(2)\ P(X) = f_{GB2}(Z)\, dZ/dX \sim\ e^{apX}(b^a + e^{aX})^{-p-q} \quad .$$

Derivation of the MP-SR model. We model the dynamics with a stochastic differential equation (SDE) in the form of

$$(3)\ dX/dt = G(X,t) + \sqrt{2\sigma}\xi = \ production\ - removal\ + \sqrt{2\sigma}\xi,$$

where both production and removal rates of damage can depend on damage level X and age t. We assume that the production and removal of damage happen much faster than the age-related change in parameters. Thus we can make the approximation that the observed damage distributions in the previous section are quasi-steady-state distributions of the SDE. The quasi-steady-state distribution can be written as the Boltzmann distribution $P(X) \sim e^{-U(X,t)/\sigma}$, where the potential function U is defined by $G(X,t) = -\partial U/\partial X$.

Using the best-fit GB2 distribution P(X) of Eq (2), we find the potential up to an irrelevant constant:

$$U(X,t) = \sigma(p+q)ln(b^a + e^{aX}) - \sigma apX \quad .$$

The two terms of this potential function naturally relate to damage production and removal terms. Thus, via differentiation of U with respect to X we find:

$$production = \sigma ap, removal = \sigma a(p+q)\, e^{ax}/(e^{ax} + e^{a\kappa}).$$

By redefining the GB2 parameters $b = e^{\kappa}, p = \eta_t/a\sigma, q = (\beta_t - \eta_t)/a\sigma$, the MP-SR model for damage dynamics in *E. coli* is given by:

$$dX/dt = \eta_t\ - \beta_t\, e^{aX}/(e^{aX} + e^{a\kappa})\ + \sqrt{2\sigma}\xi.$$

The GB2 parameters that best fit the experimental data show that p/(p+q) rises approximately linearly with time (Fig. 1F) and that b and a remain approximately constant. We conclude that

620 the observed damage distributions are well-described by an SR-type process with $\eta_t = \eta t$ and

621 $\beta_t = \beta$, as in Eq 1.

622

Supplementary materials:

Table of Contents

S1 Estimated of experimental noise

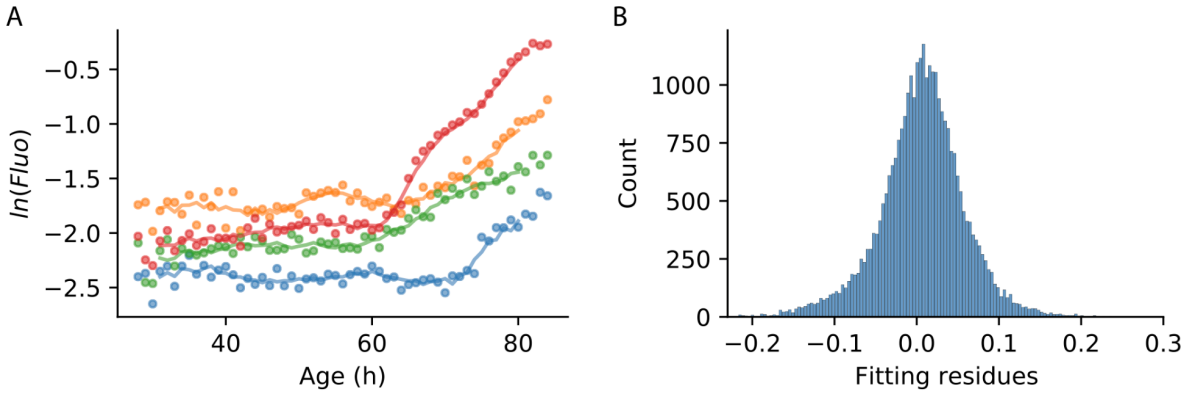

Figure S1 Estimation of experimental noise. (A) Data derived from time-lapse microscopic images (dots) is assumed to be composed of a relatively slow moving signal (curves) and sequentially independent multiplicative experimental noise. The curves are moving averages of 7h with min and max value removed. The difference between these curves and the raw data in log scale, i.e. the fitting residues, is our estimate of experimental noise. (B) Histogram of the fitting residues. The mean of this distribution is approximately zero, 0.02+/-0.03XX, and the standard deviation approximates the magnitude of experimental noise, about 5.5%. The left half of this distribution was used to estimate the magnitude of the experimental noise, because the distribution is skewed to the right due to the generally rising trends of PI signal.

S2 Best fit distribution functions to experimental damage distributions

In this section we provide details for the fits of the 15 distribution functions to the experimental *E. coli* damage distributions at different ages. We provide the KS statistic (Table S1) and p-value (Fig S2), where a higher KS p-value (bluer colors) means a better fit. The distributions are ordered according to goodness of fit (average log p-value).

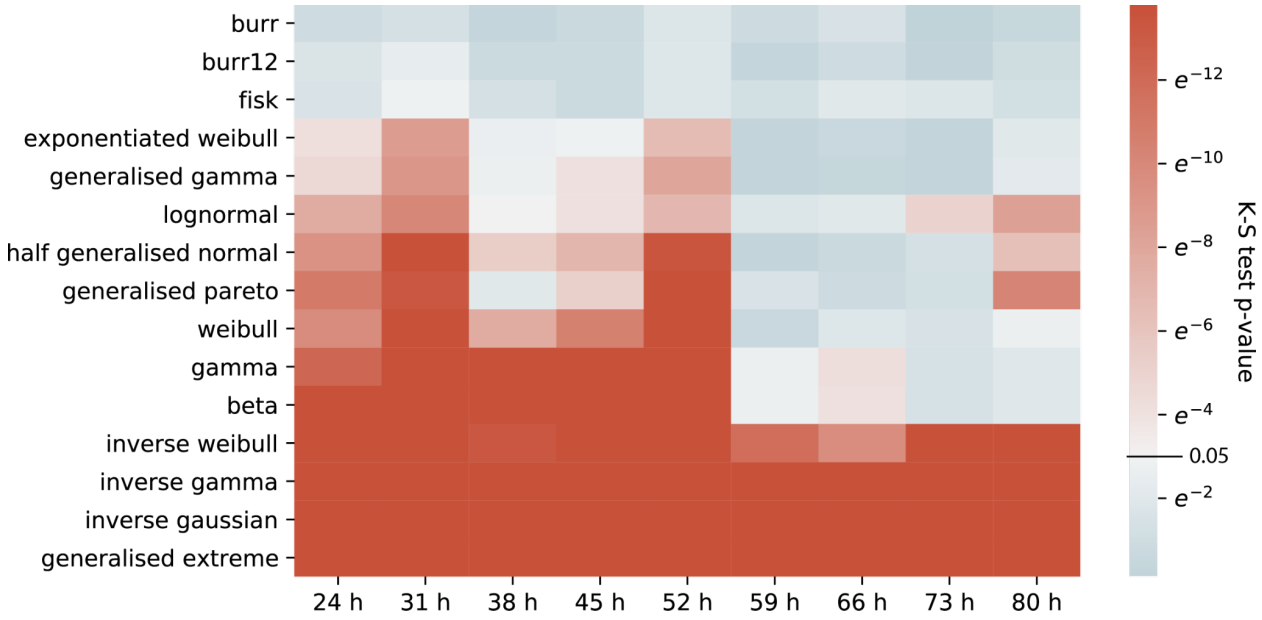

Figure S2 KS test p-values for 15 distribution functions to the marginal damage distributions at different timepoints. Functions are ordered by mean p-value.

Model	K-S statistic								
	24.5h	31.5h	38.5h	45.5h	52.5h	59.5h	66.5h	73.5h	80.5h
burr	0.042	0.046	0.035	0.038	0.047	0.048	0.046	0.027	0.038
burr12	0.051	0.057	0.041	0.038	0.048	0.038	0.040	0.029	0.046
fisk	0.049	0.061	0.048	0.038	0.048	0.052	0.051	0.051	0.048
exponentiated weibull	0.073	0.098	0.062	0.060	0.080	0.037	0.034	0.031	0.058
generalized gamma	0.076	0.101	0.063	0.069	0.088	0.036	0.033	0.032	0.059
lognormal	0.095	0.106	0.067	0.069	0.082	0.060	0.051	0.078	0.106

half generalized normal	0.104	0.129	0.085	0.087	0.112	0.036	0.036	0.045	0.093
generalized pareto	0.112	0.121	0.056	0.077	0.115	0.058	0.039	0.044	0.116
weibull	0.106	0.142	0.099	0.106	0.129	0.043	0.050	0.049	0.064
gamma	0.118	0.166	0.141	0.150	0.153	0.070	0.069	0.048	0.057
beta	0.127	0.166	0.140	0.149	0.156	0.070	0.068	0.048	0.057
inverse weibull	0.152	0.284	0.129	0.136	0.153	0.134	0.100	0.140	0.202
inverse gamma	0.214	0.461	0.185	0.239	0.253	0.223	0.135	0.195	0.281
inverse gaussian	0.220	0.784	0.201	0.280	0.279	0.326	0.152	0.216	0.316
generalized extreme	0.376	0.394	0.373	0.374	0.396	0.369	0.372	0.372	0.387

Table S1 Kolmogorov-Smirnov (KS) test statistics for the 15 distribution functions compared to the marginal damage distributions at different timepoints.

S3 Shortening twilight in the *E. coli* dataset

We follow the pioneering work of Stroustrup et al and explore the question of twilight, the time from a measurable age related phenotype to the time of death [24]. Suppose there is a measurable age-related phenotype that is equivalent to damage crossing a threshold X1. If we define twilight [23] as the remaining lifespan after the threshold is crossed , the question is whether twilight shortens or lengthens with the age at which the threshold is crossed.

The SR model predicts that twilight shortens with age on average (Fig S3ABC). Equivalently, the time to cross X1, denoted t_1, should be positively correlated with time of death t_d, but with a correlation coefficient less than one (Fig S3B).

The reason for the shortening twilight is that the damage production term ηt rises with age. Individuals that cross X1 at early times have a low production term. It takes them longer to reach the death threshold than those crossing X1 at late times. Thus there is a negative correlation between t_1 and remaining lifespan (Fig S3C). This prediction is borne out by the *E. coli* dataset (Fig S3D). A similar effect was observed in aging *C. elegans* [24].

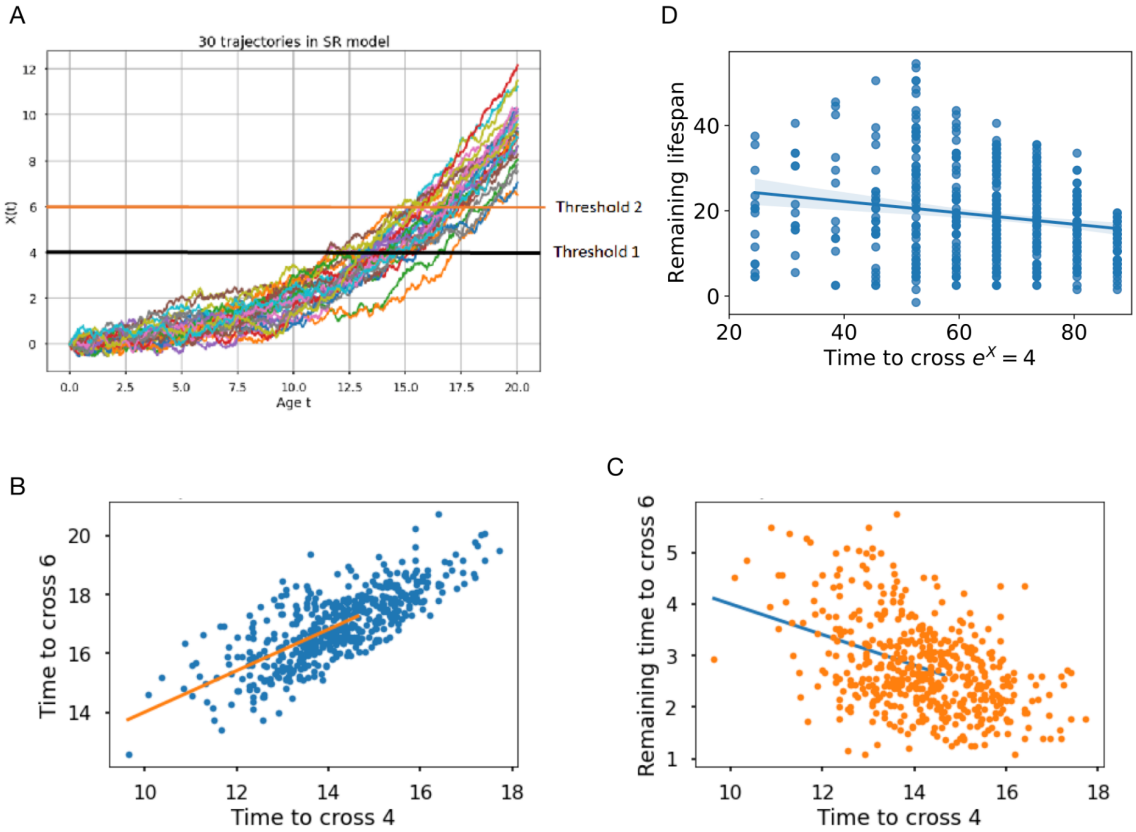

Figure S3 *E. coli* shows shortened twilight at old age. (A) SR model simulation with parameters $\eta = 0.1, \beta = k = 1$. Thresholds are 4 and 6. (B) Time to cross the two thresholds is correlated but with slope less than 1 (regression slope ~ 0.7). (C) Remaining lifespan (remaining time to

cross threshold 6 after threshold 4 is crossed) drops with time to cross threshold 4. (D) Correlation of remaining lifetime with time to cross a damage threshold of e^X=4 in the *E. coli* dataset. Regression line is y=-0.13x+27.5.

S4 Analytical properties of the MP-SR model

Here, we derive the risk of death of the MP-SR model analytically, using Kramer's approximation.

The model equation is:

$$dX/dt = \eta t - \beta\, e^{aX}/(e^{aX} + e^{a\kappa}) + \sqrt{2\sigma}\xi$$

One can write this in terms of a potential function $U(X,t)$ (Fig. 4C) :

$$dX/dt = -\partial U(X,t)/\partial X + \sqrt{2\sigma}\xi,$$

where the potential function is:

$$U(X,t) = -\eta t X + \beta/a\, ln(e^{a\kappa} + e^{aX})$$

We model mortality as the first time when $X > X_c$. Thus, death time is a first-passage time of the MP-SR model variable *X*. To estimate the risk of death, i.e. hazard rate, we apply the Kramer approximation [21,22] for the first passage time:

$$h(t) \approx \frac{\sqrt{U''(X_0)U''(X_C)}}{2\pi}\, e^{-\frac{U(X_C)-U(X_0)}{\sigma}}$$

Where X_0 is the steady state of the system.

To arrive at Gompertz law, one needs $-\frac{U(X_c)-U(X_0)}{\sigma}$ to increase linearly with age. This is indeed the case:

$$-\frac{U(X_c)-U(X_0)}{\epsilon} = t\eta\sigma^{-1}(X_c - X_0) + \beta a^{-1}\sigma^{-1}[z(X_0) - z(X_c)],$$

Where $z(x) = ln(e^{ax} + e^{a\kappa})$. If the quasi-steady-state X_0 is constant and much smaller than Xc, as it is at young ages, one obtains the Gompertz hazard rate $h(t) \sim e^{\frac{\eta X_c}{\sigma}t}$ with the Gompertz slope $\eta\sigma^{-1}X_c$.

721 However, the quasi-steady state X_0 does increase with age, and rises more rapidly at late ages
722 approaching Xc (Fig. 4B). Thus the hazard rate is only approximately Gompertzian, especially at
723 late ages. If we use the quasi-steady state $X_0 = ln(\frac{t\eta}{\beta - t\eta})/a$ to calculate the hazard rate, we get
724 a more complicated, non-Gompertzian formula, plotted in Fig. S4. This more realistic result
725 shows late-age deceleration when compared with the Gompertz law. This deceleration is
726 indeed observed experimentally for *E. coli* in similar conditions [4].
727

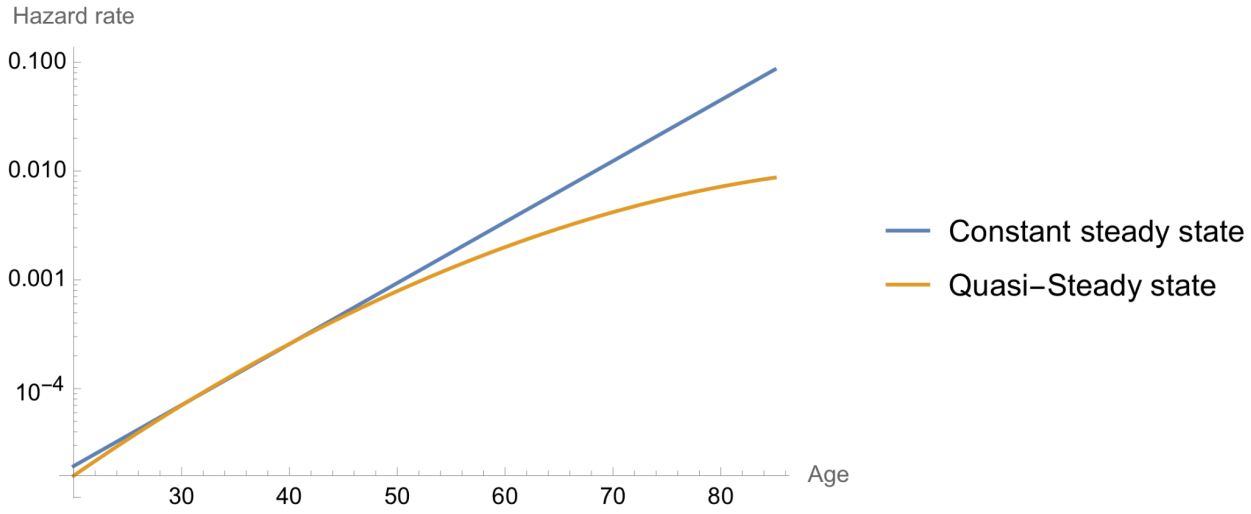

728
729
730 **Figure S4** Analytically calculated hazard rate of the MP-SR model using Kramer's
731 approximation. The two curves follow different assumptions: Blue curve shows Gompertz law,
732 under the constant steady state assumption. Yellow curve uses a quasi-steady state that
733 changes with age and shows late-age deceleration.

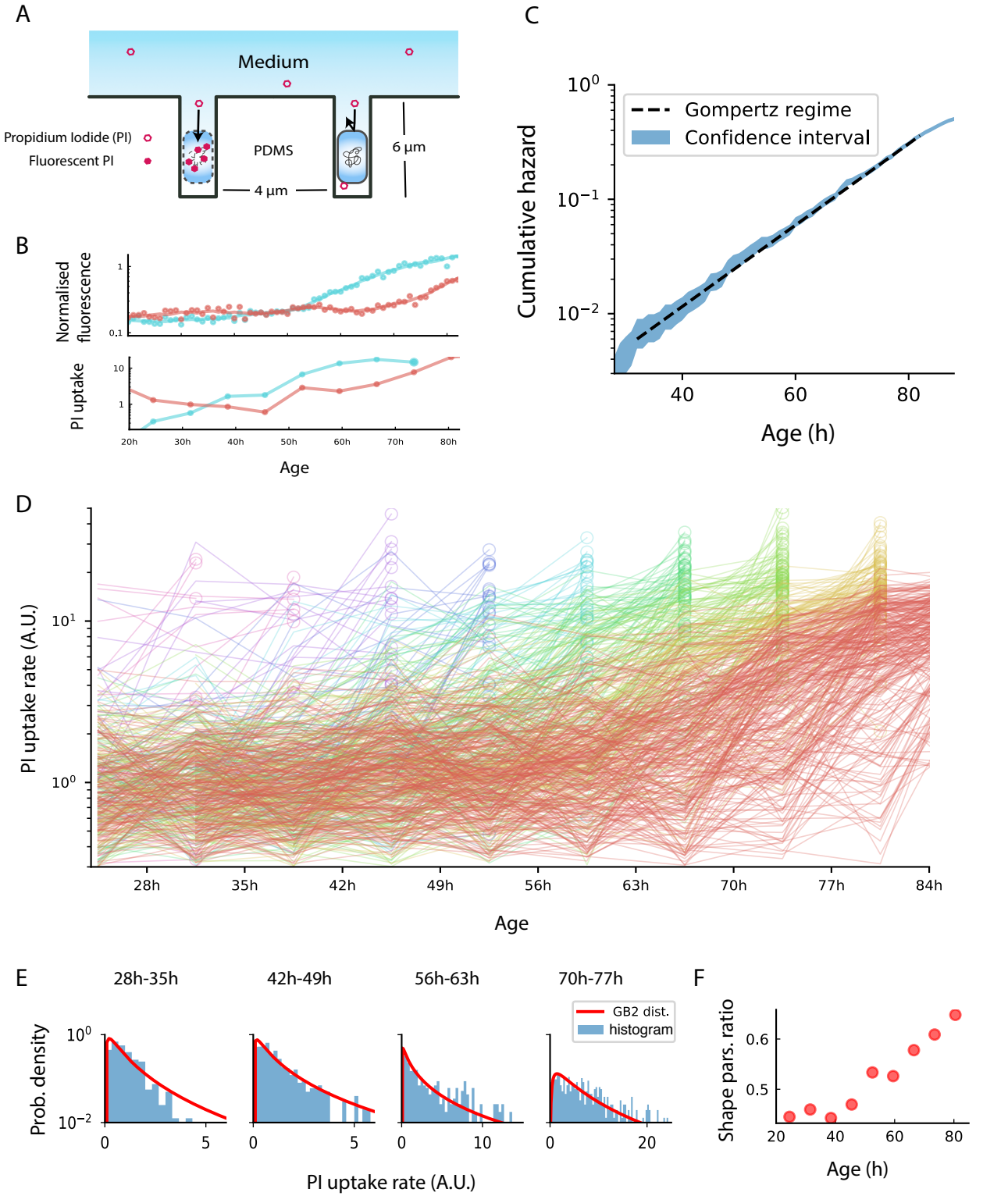
A
Medium
Propidium Iodide (PI)
Fluorescent PI
PDMS
4 µm
6 µm
B
Normalised fluorescence
PI uptake
20h
30h
40h
50h
60h
70h
80h
Age
C
Cumulative hazard
Gompertz regime
Confidence interval
Age (h)
D
PI uptake rate (A.U.)
28h
35h
42h
49h
56h
63h
70h
77h
84h
Age
E
28h-35h
42h-49h
56h-63h
70h-77h
GB2 dist.
histogram
Prob. density
PI uptake rate (A.U.)
F
Shape pars. ratio
Age (h)

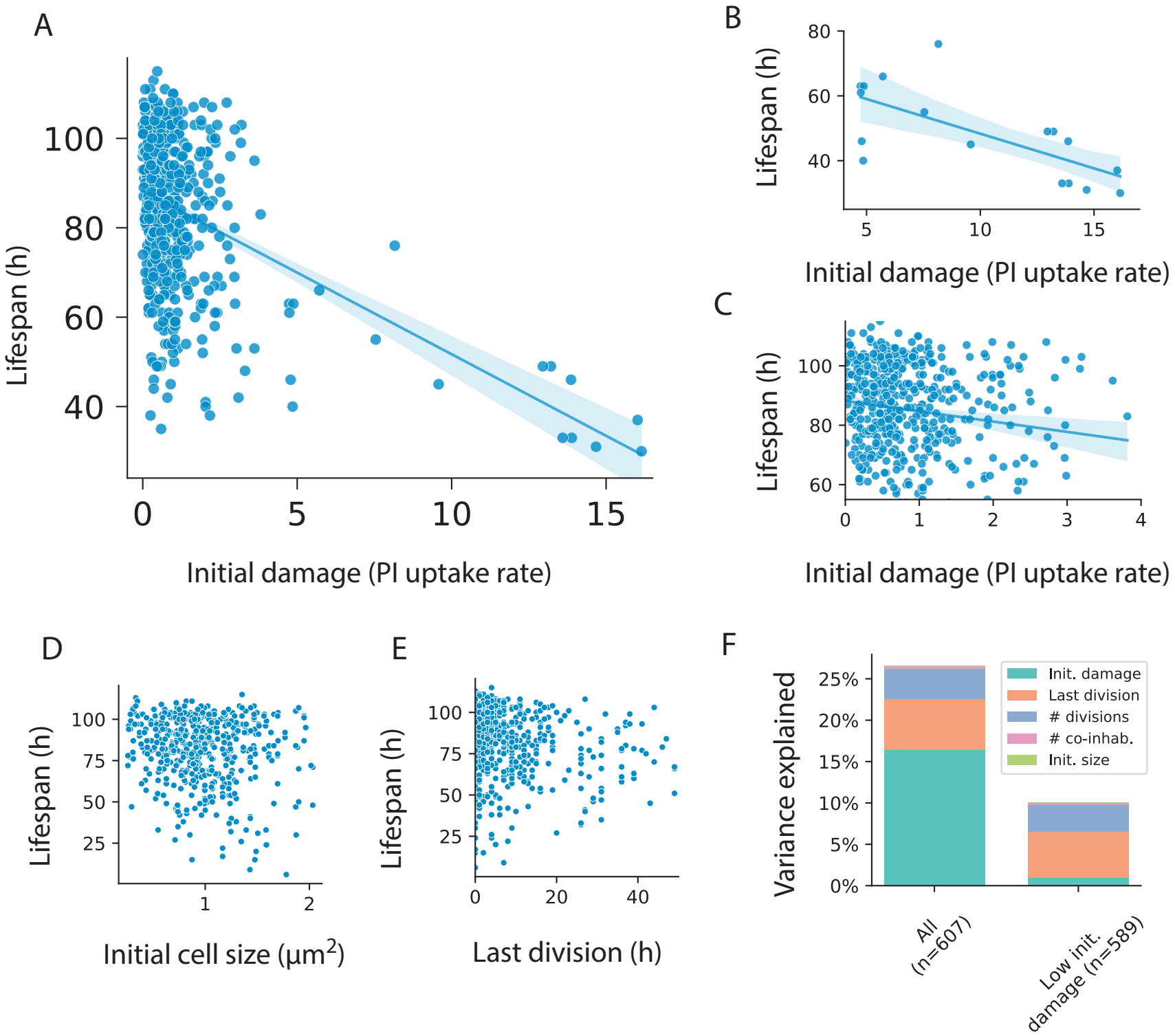
A
Lifespan (h)
100
80
60
40
0
5
10
15
Initial damage (PI uptake rate)
B
Lifespan (h)
80
60
40
5
10
15
Initial damage (PI uptake rate)
C
Lifespan (h)
100
80
60
0
1
2
3
4
Initial damage (PI uptake rate)
D
Lifespan (h)
100
75
50
25
1
2
Initial cell size (μm²)
E
Lifespan (h)
100
75
50
25
0
20
40
Last division (h)
F
Variance explained
25%
20%
15%
10%
5%
0%
Init. damage
Last division
divisions
co-inhab.
Init. size
All (n=607)
Low init. damage (n=589)

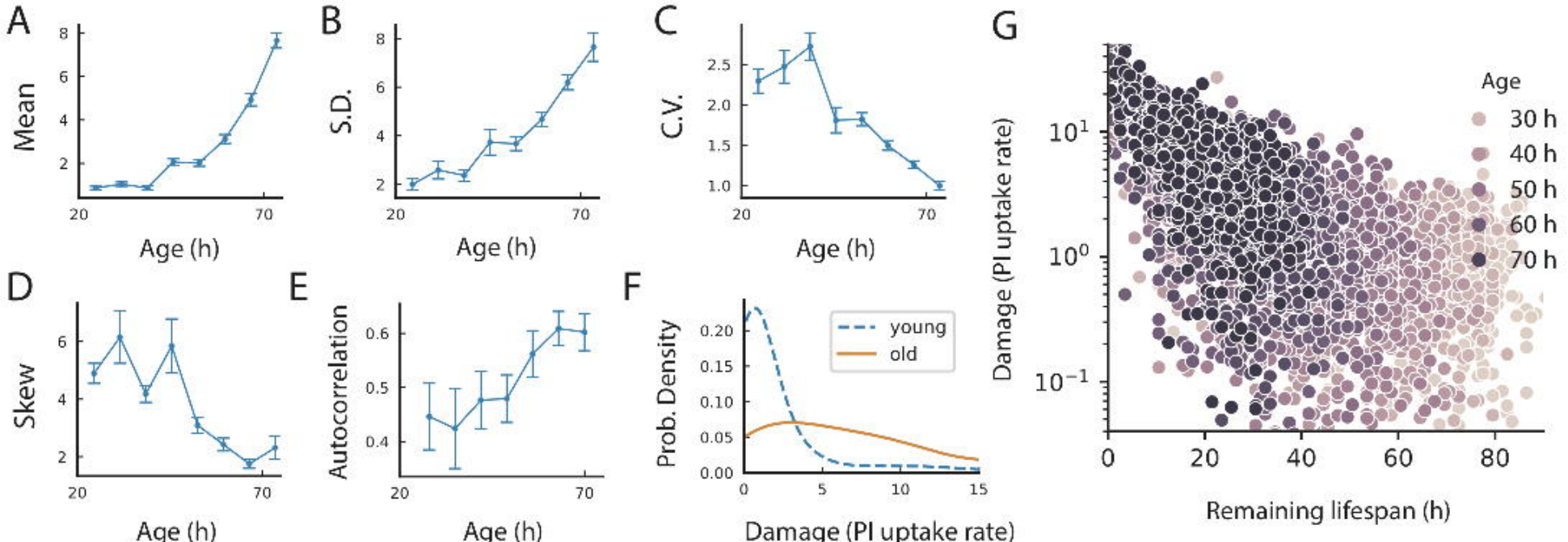
A
Mean
Age (h)
B
S.D.
Age (h)
C
C.V.
Age (h)
D
Skew
Age (h)
E
Autocorrelation
Age (h)
F
Prob. Density
young
old
Damage (PI uptake rate)
G
Damage (PI uptake rate)
Age
30 h
40 h
50 h
60 h
70 h
Remaining lifespan (h)

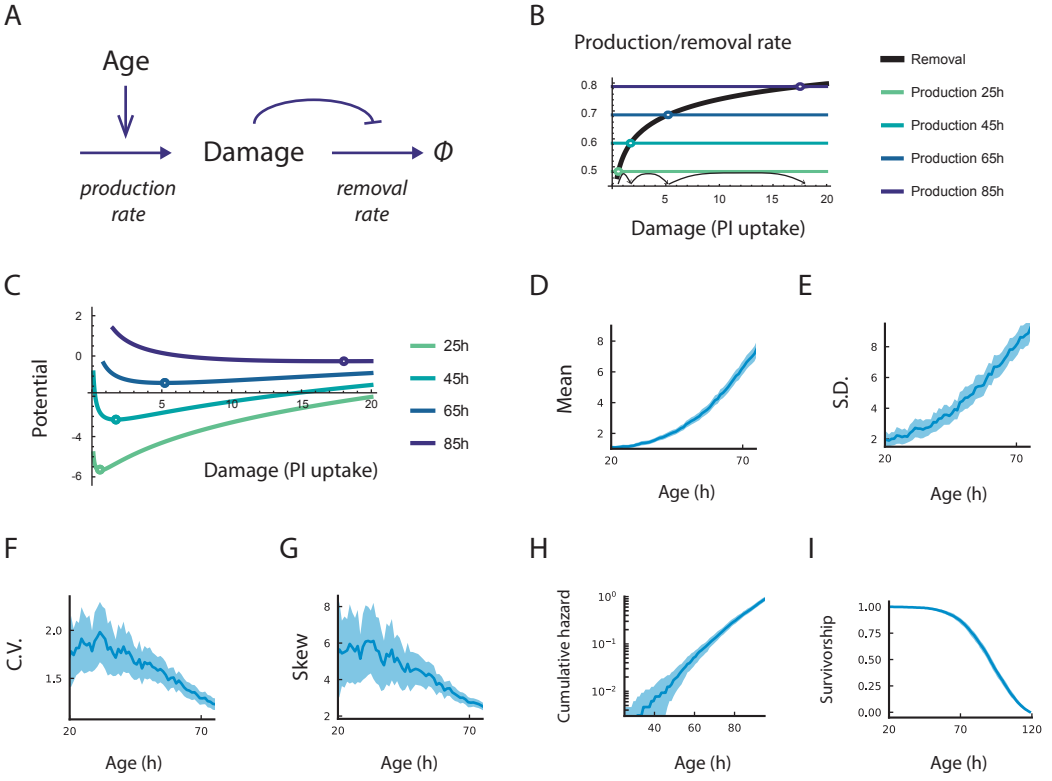
A
Age
Damage
Φ
production rate
removal rate
B
Production/removal rate
Removal
Production 25h
Production 45h
Production 65h
Production 85h
Damage (PI uptake)
C
Potential
25h
45h
65h
85h
Damage (PI uptake)
D
Mean
Age (h)
E
S.D.
Age (h)
F
C.V.
Age (h)
G
Skew
Age (h)
H
Cumulative hazard
Age (h)
I
Survivorship
Age (h)